Limits of Coupling Efficiency into Hollow-core Antiresonant Fibres

Viktor Zuba, *Student Member, IEEE,* Hans Christian H. Mulvad, Radan Slavík, *Senior Member, IEEE, Fellow, OSA,* Hesham Sakr, Francesco Poletti, *Member, IEEE,* David J. Richardson, *Fellow, IEEE, Fellow OSA,* and Eric Numkam Fokoua, *Member, IEEE, Senior Member OSA*

***Abstract*—We theoretically explore the fundamental limits on the efficiency of coupling light into hollow-core antiresonant fibres. We study in particular the coupling of a free-space Gaussian beam to the guided modes of one of the most successful antiresonant fibre (ARF) geometries, the the nested antiresonant nodeless fibre (NANF). Through finite element simulations, we study the effect of the geometrical parameters of the fibre on the coupling efficiency, showing that coupling into the fundamental LP_{01}-like mode is typically maximized around 96-98 % when the incident beam waist is about 70 % of the core diameter. We find that due to the nature of antiresonance guidance, higher coupling efficiencies are achieved for fibres operating in the second antiresonant window (or generally even-numbered windows) than in those operating in the fundamental antiresonant window (or generally odd numbered windows), although the difference between even and odd decreases with the order of the window. We verify this theoretical finding experimentally with precise measurements of coupling efficiency into two NANFs operating in first and second windows, respectively. Our results which consistently show a steady 1.4 percentage point higher coupling efficiency for the second window fibre imply that such fibers may be the most suitable candidates for applications such as laser delivery which require up to a few hundred meters of fiber.**

***Index Terms*—Coupling efficiency, Optical fibre, Hollow-core fibre, Anti-resonant fibre, Single-mode fibre, Beam delivery**

I. Introduction

RECENT fast-paced progress in the development of hollow-core antiresonant fibre (HC-ARF) technology, culminating in the reduction of their attenuation to $0.174\,\mathrm{dB/km}$ [1], is rapidly establishing these fibres as an attractive option to replace existing solid-core optical fibres in a host of applications. These range from high power laser delivery [2], [3], to sensing [4], [5], and telecommunications [6]–[8] where its first commercial deployments have now been reported [9]. In addition to this sustained progress in loss reduction – which theory predicts can be lowered still – the case for these fibres is even more compelling given their attractive properties of low optical non-linearity [10], near vacuum latency, environmental insensitivity and polarization purity [11], to name just a few. All of these unique properties bring significant improvements in numerous applications, whilst unlocking many new ones where vacuum-like guidance in a long thin and flexible waveguide can be a radical game changer.

An important enabling step towards wider adoption of hollow-core optical fibre technology is the ability to efficiently interface the fibres with existing components, including light sources and solid-core fibre based devices. Let us consider as an example, the case of precise laser based material processing. Here, the optical power must be delivered flexibly from a high brightness laser source to a work piece [12]. The efficiency with which the laser light is launched into the fibre is an important consideration. Solid-core fibres (SCFs) have been used already with great success in such applications [13], but they ultimately face fundamental limitations due to the fact that the most intense part of the laser light is propagated through the solid core material.

As the optical power increases, it gives rise to nonlinear light-matter interactions which cannot be neglected. Based on the type of laser radiation – i.e. pulsed or continuous wave (CW) – optical nonlinearities, such as the Kerr effect, stimulated Brillouin or Raman scattering (SBS and SRS, respectively) become important parasitic effects with unwanted consequences for the desired application [2]. More intense laser beams can cause damage to the fibre coating if the heat generated at the initial section of fibre is not managed appropriately [3]. Finally, the ultimate physical limit is reached when the incident optical power is higher than the glass damage threshold, causing irreversible breakdown damage to the fibre. Clearly, these effects can be overcome by employing HC-ARFs in which light is confined and guided in a hollow region, effectively reducing the overlap between the guided beam and the glass structure by $4-5$ orders of magnitude [14]. This is illustrated by recent demonstrations of near-infrared (central wavelength $\lambda_0 \approx 1060-1080\,\mathrm{nm}$) CW laser light delivery through HC-ARFs [3], [15], including the breakthrough result of transmitting $1\,\mathrm{kW}$ of power over a $1\,\mathrm{km}$ long nested antiresonant nodeless fibre (NANF) [2].

In their most successful embodiments, ARFs consist of a number of non-contacting thin glass tubes, nested, double nested or otherwise, surrounding a central hollow core and attached on the inside of a thicker silica jacket tube. Figure 1 shows example cross-sections of ARFs fabricated by our team at the University of Southampton. As can be appreciated, the fibre's geometries – and by extension their supported mode fields too – lack the same circular symmetry that is associated with free space beams or those emerging from solid-core fibres

Manuscript received ... placeholder. *(Corresponding author: Viktor Zuba, email: V.Zuba@soton.ac.uk)*

Viktor Zuba, Hans Christian H. Mulvad, Radan Slavík, Hesham Sakr, Francesco Poletti, David J. Richardson, and Eric Numkam Fokoua are with the Optoelectronics Research Centre, University of Southampton, SO17 1BJ Southampton, U.K..

Digital Object Identifier: ... .

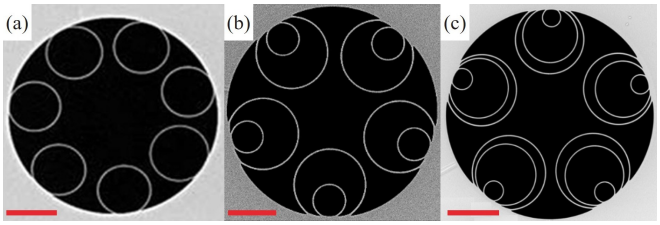

Fig. 1. Typical scanning electron micrographs (SEM) of some antiresonant hollow core fibres: (a) Simple tubular Antiresonant Fibre (ARF) [10], (b) Nested Antiresonant Nodeless Fibre (NANF) used in this article, (c) Double Nested Antiresonant Nodeless Fibre (DNANF) [1]. The red scale bars in of each of the images correspond to 20 µm, respectively.

and related components. It will be shown that whilst the a priori expectation of this symmetry mismatch imposing some limitation on the coupling efficiency between such beams and the fibre's fundamental mode (FM) holds true, the maximum achievable coupling efficiency is not too dissimilar to values achieved in standard fibres.

With the already demonstrated low loss levels and with the expectation of even lower losses still to come, the coupling loss into the fibre will dominate the overall power loss in applications requiring relatively short fibre lengths (e.g., tens to hundreds of meters in most high-intensity laser beam delivery applications). Besides this undesirable coupling loss, the power that escapes at launch into the fibre is most likely to generate heat and lead to end-face damage [16], or some other type of fibre failure [3], [17], particularly when operating with high laser powers.

Several works have investigated various practical methods of optimizing launch into hollow-core fibres (HCFs): either via free-space coupling into bare HCFs [18], splicing end-caps to HCFs [19], direct splicing of HCFs and commercial SCFs [20], gluing intermediate graded-index elements [21], [22], or more delicate ones, such as employing tapered nanospikes [23], or silica balls [24]. However, no study has hitherto established the fundamental limits governing this coupling efficiency (CE) and whether it can be optimized through the design of the fibre cross-section itself.

In this paper, we theoretically investigate the CE between a free-space Gaussian beam and the modes of an idealized NANF. We find the coupling to the fundamental LP_{01} mode to be maximized (over 97 %) when the incoming beam diameter is approximately 70 % the core diameter. We perform detailed numerical studies of the impact of the fibre's geometrical parameters on the coupling efficiency. We find that due to the odd or even number of sign changes in the mode field as it crosses the cladding membranes when the fibre operates in odd or even numbered antiresonant windows, the maximum achievable coupling efficiency in even-numbered antiresonant windows is higher [25]. In particular, the difference in coupling efficiencies between similar idealized fibres operating in the first and second window is predicted to be as high as 1.3 percentage point (p.p.), or 1.4 % relative improvement. When we assume that comparable loss levels have been achieved in fibres operating in the first and second window at the important laser wavelength of 1064 nm for example, this difference in CE can be significant. Assuming the same attenuation for such pairs of fibres, second window fibres provide the lowest total loss, and thus are the ultimate choice for many applications. Furthermore, their thicker glass membranes make them more resilient, less prone to handling related damage, while also showing more resilience to fluctuations during the fibre drawing process [26]. This difference in CE between first and second window fibres is then verified experimentally with careful measurements of the coupling efficiency into NANFs operating in the first and second antiresonant windows, respectively, at the aforementioned 1064 nm wavelength [27].

This paper is organized as follows. Section II introduces the theoretical background essential for discussions regarding the different optical transmission windows of the ARFs, as well as efficient excitation of their optical modes. The methodology of the experiments is detailed in Section III. In Section IV, results of the measurements are compared to theoretical expectations, and finally, Section V concludes the paper.

II. Theoretical analysis of light coupling into ARFs

We consider in this section how an incoming mode field which we denote $|\psi\rangle$ is coupled to the modes of the HC-ARF denoted by $|\psi_k\rangle$. The modes supported by the fibre consist of the discrete core-guided modes, cladding modes and the continuum of radiation modes which form a complete and orthogonal set. Though the core-guided modes are leaky, they still approximately satisfy the power orthonormality relation [28]:

$$\iint \vec{z} \cdot (\mathbf{E}_k^* \times \mathbf{H}_{k'} + \mathbf{E}_{k'} \times \mathbf{H}_k^*)\, dA = \delta_{k,k'} \tag{1}$$

where $\mathbf{E}_k$ and $\mathbf{H}_k$ represents the the electric and magnetic field distributions of the mode $|\psi_k\rangle$ and $\delta_{k,k'}$ is the Kronecker delta. Because the modes of hollow-core fibers are leaky, the power orthonormality relation of Equation (1) only holds approximately. Although more rigorous orthogonality relations have been derived for leaky modes [29], [30], we find that the low-loss of current HC-ARFs affords the use of Equation (1) without loss of accuracy.

Following the work of Marcuse [31], the incident field $|\psi\rangle$ with electric and magnetic field vectors $\mathbf{E}$ and $\mathbf{H}$ can be expressed as a linear combination of the modes $|\psi_k\rangle$ so that:

$$\mathbf{E} = \sum_k c_k \mathbf{E}_k, \quad \mathbf{H} = \sum_k c_k \mathbf{H}_k \tag{2}$$

where the coefficient c_k represents the excited amplitude of mode $|\psi_k\rangle$. By combining Equations (1) and (2), the coefficient c_k is obtained as:

$$c_k = \iint \vec{z} \cdot (\mathbf{E} \times \mathbf{H}_k^* + \mathbf{E}_k^* \times \mathbf{H})\, dA \tag{3}$$

It follows, using Equations (1) and (3) that the total power P carried by the incident field is simply:

$$P = \sum_k |c_k|^2 \tag{4}$$

so that when $P = 1$, the power coupling efficiency – referred to simply as coupling efficiency (CE) in the following – into mode $|\psi_k\rangle$ is given by $|c_k|^2$.

It is well-known that the large core sizes of antiresonant fibres result in them supporting multiple transverse modes $|\psi_k\rangle$, although their structure can be engineered to achieve effective single-mode operation [32]. Rigorously speaking, the modes $|\psi_k\rangle$ are vector modes and leaky in nature. For simplicity however, we will adopt throughout the paper the LP terminology to refer to groups of degenerate or nearly degenerate fibre modes so that the LP_{01} for example is understood to refer to the pair of fundamental HE_{11} modes, the LP_{11} group made up of the TE_{01}, TM_{01} and the degenerate HE_{21} modes, etc.

Using Equation (3), we now consider how an incoming free-space TEM_{00} Gaussian-like laser beam would excite the modes of a NANF featuring 5 sets of nested tubes - one similar to the illustration in Figure 1 (b). NANF samples with the same number of tubes will be also used for the experimental verification of expectations predicted by theory in the later sections. We consider such an incident beam to be linearly polarized along the x-axis so that the electric and magnetic field vectors at the focus $z = 0$ are given by:

$$\begin{aligned} \mathbf{E}\,(z=0) &= \vec{x}Ae^{-\frac{x^2+y^2}{w^2}} \\ \mathbf{H}\,(z=0) &= \vec{y}Be^{-\frac{x^2+y^2}{w^2}} \end{aligned} \tag{5}$$

where w is the beam waist of a Gaussian beam.

For the NANFs considered here, following the parameter definitions as shown in Figure 2 (a), the core diameter is fixed at $2a = 30\,\mu$m, the cladding membranes have thickness $t = 360\,$nm and the gaps between the larger tubes is $d = 4.0\,\mu$m. The size of the nested tube is chosen so that $z/a = 0.95$, where z denotes the distance between the inner and outer tubular elements. These parameters are similar to those of the fabricated fibres used in the experiments described later. Assuming that the incident beam and NANF are perfectly aligned, we show in Figure 2 (c) the power coupling efficiency for the first four mode groups – illustrated in (b) – supported by the NANF. The coupling efficiency is shown here in the form of coupling loss in decibels, i.e., $-10 \cdot log(|c_k|^2)$, as a function of the ratio between the beam waist w and the core radius a. This calculation was performed at the wavelength of $\lambda = 1064\,$nm, corresponding to a normalized frequency $f = 0.71$ in the first antiresonance window – we recall that $f = 2t\sqrt{(n^2-1)}/\lambda$, n being the refractive index of the glass [25].

We see that for the FM, the coupling loss is minimized when the incident mode field diameter $2w$ is approximately 70 % of the core diameter $2a$. We define this value for which the coupling from a free space Gaussian beam is maximized to be the mode field diameter (MFD) of the fibre. The minimum coupling loss achieved in this case is $0.13\,$dB, corresponding to a coupling efficiency of ~97 %. Looking at the HOMs, we observe that the LP_{11} and LP_{21} modes receive a negligible fraction of the incident power in the region of $-110\,$dB to $-50\,$dB coupling levels, respectively, as one may expect due to the symmetry mismatch with the incoming Gaussian beam. Because of its azimuthal symmetry, the coupling into the LP_{02} mode is of the order of $-20\,$dB. As HOMs typically suffer from much higher coupling loss than the FM, these results show that with careful alignment, it is possible to achieve effective single-mode coupling into ARFs, because after a few meters of propagation the already low fraction of power coupled into HOMs would be effectively lost.

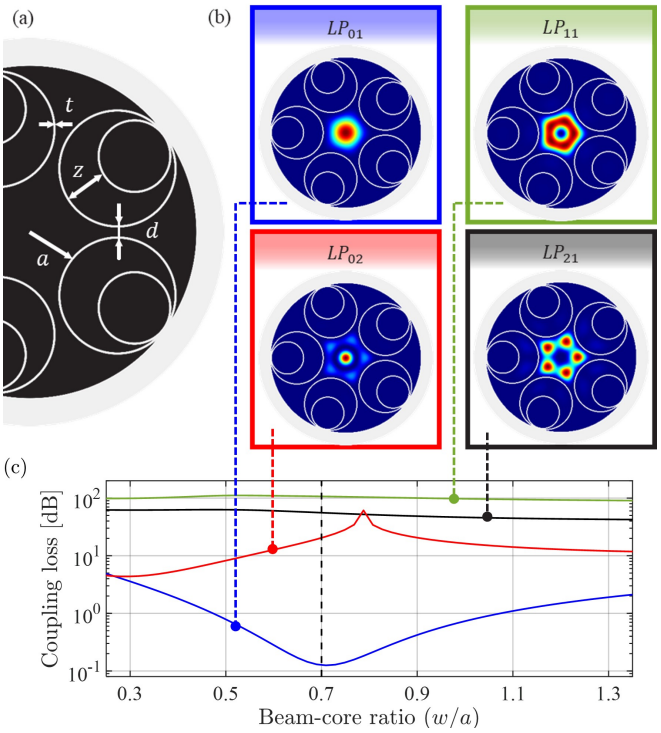

Fig. 2. (a) Schematic cross section of a typical 5-tube NANF microstructure, including the main geometrical parameters: a: core radius, t: membrane thickness, d: separation of outer tubes, z: inner and outer tube separation, (b) Illustration of the normalized electric field distribution of the first 4 mode groups (note that although we use the LP nomenclature for simplicity, these are vector modes), (c) Corresponding coupling loss values of the respective mode group, as a function of the beam-core ratio w/a, where w is the beam waist of a Gaussian beam. In case of ideal coupling (marked with vertical dashed line for a 0.7 beam-core ratio), most of the field is coupled into the LP_{01} (blue curve) mode, while the other higher order modes receive only a fraction of it, -20 dB, -50 dB, -110 dB for the LP_{02}, LP_{21} and LP_{11} modes, (red, black and green curves) respectively.

In what follows, we focus our analysis on the coupling to the fundamental mode alone. We first examine how the CE and the MFD defined above change with wavelength – or analogously with normalized frequency. We plot both quantities in Figure 3 (a) and (b) as a function of the normalized frequency across the first three antiresonant windows. It can be appreciated that the MFD shows fano-resonance-like behavior near the resonant wavelengths, i.e., $f = 1, 2, ...$, but remains around the 70 % mark at normalized frequencies corresponding to regions with low coupling and propagation losses. Noticeably, the minimum coupling loss presents a clear dependence on the order of the antiresonance window. As shown in Figure 3 (c), it reaches a minimum of ~0.13 dB in the first window, ~0.07 dB (~98.4 % coupling efficiency) in the second window and ~0.09 dB in the third. Note that the seemingly negligible $0.06\,$dB difference

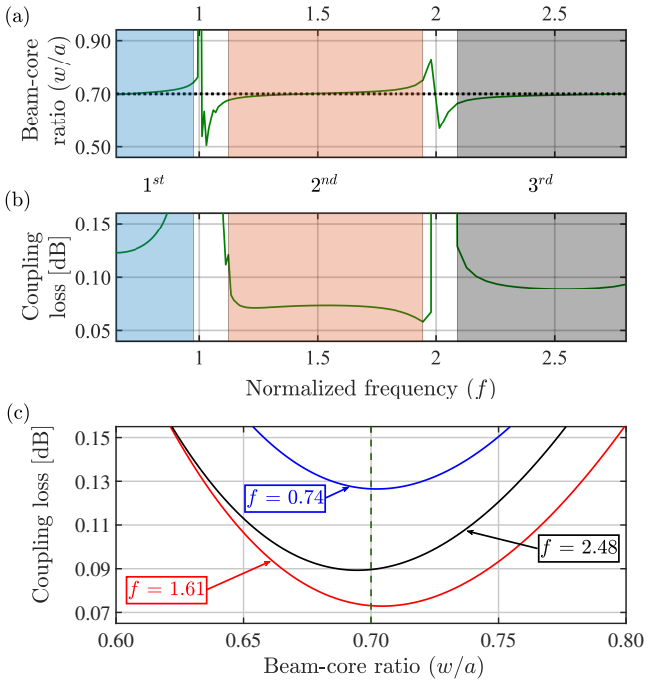

Fig. 3. Coupling between free space Gaussian beam into the fundamental mode of a 6-tube NANF as a function of normalized frequency: (a) incident beam waist to core size ratio w/a for which coupling loss is minimized as a function of the normalized frequency f, (b) corresponding minimum coupling loss as the function of the normalized frequency f. Regions highligthed in blue, red and gray colours correspond to the 1st, 2nd and 3rd order antiresonant windows, respectively. (c) Coupling loss versus normalized incident between waist at selected normalized frequencies within the first (blue), second (red) and third (black) anitiresonant windows. Note how the best coupling is achieved at around w/a ~0.7, highlighted by the vertical dashed line.

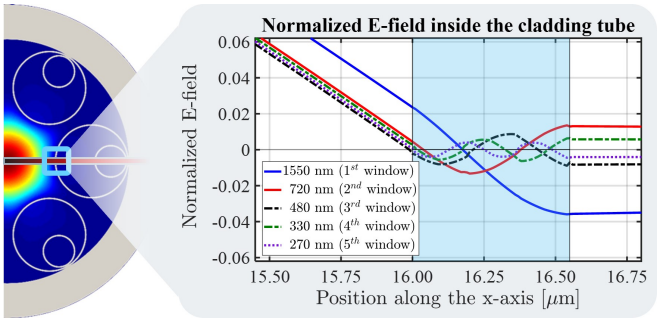

Fig. 4. Normalized electric field distribution of the fundamental LP_{01} mode of a typical 6-tube NANF. Highlighted are the curves of the x-component of the electric fields of different wavelengths, corresponding to different f normalized frequencies or optical windows, along the marked cut of the fibre cross-section. It can be seen that the electric field changes sign an m-number of times inside the cladding membrane (illustrated by the light-blue section), where m is the order of the respective transmission window. These curves show an increased overlap with a strictly-positive Gaussian distribution for the case of even-numbered windows, with the best fit correlated to the 2nd order.

in coupling loss between the first and second window is comparable to the loss incurred by propagation in as long as 350 m for a fibre with attenuation of 0.174 dB/km.

To examine the origin of this dependence on the order of the antiresonant window, we take a closer look at the mode-field distribution. We plot in Figure 4 the x component of the electric field vector in the fibre cross-section, with a cut taken along the diameter that bisects a cladding tube, focusing around the cladding membrane. We see that in the first window ($f = 0.74$), the electric field changes sign once across the membrane, but does so twice when operating in the second window ($f = 1.74$). This means that in the second window, the electric field distribution of the mode is better matched to that of the incident Gaussian beam whose magnitude does not change sign. By extension, we can see that the coupling efficiency – which is the overlap between the two fields – will be greater in even-numbered windows than in odd-numbered windows, though the discrepancy decreases as the order of the window increases.

We next turn our attention to investigating the impact of other geometric parameters on the coupling efficiency and MFD, since they potentially have a direct impact on the modal electric field distribution. First we examine the impact of the gap between the cladding tubes. Using a 6-tube NANF operating in the first antiresonant window as an example, we change the gaps d from 1 to 5.5 µm, while maintaining the core radius a and the thickness of the tubular elements t constant. This means that the inner radius of the microstructured region becomes smaller as the gaps are increased – as depicted in Figure 5 (a). Note that by doing so, the loss of the fibre increases markedly. As the gap increases, we note an increase in the mode-field diameter which may be expected given that the mode field expands to the spaces between the tubes. At the same time, we see that the coupling loss experiences a very slight decrease (i.e. the CE increases). This can be understood from the preceding analysis. As the gap increases, the size of the cladding tubes reduces accordingly implying a smaller region over which there is a sign mismatch between the incident Gaussian field and the mode field distribution.

Secondly, to investigate the impact of mode shape, we now keep the parameters d, a, t constant, but alter the symmetry of the mode field by changing the number of cladding tubes N. Doing so changes the number of modes supported in the structure as well as the loss of the fibre [33], [34]. Unsurprisingly, increasing the number of cladding tubes results in a more circular mode field distribution, as well as a smaller MFD, which in turn leads to a lower coupling loss (higher CE), as can be seen in Figure 5 (b).

From the understanding gained from the analysis above, we can predict the effect of other structural parameters. Considering operation in the first antiresonant window, we can see for example that by increasing the size of the larger cavity (i.e., increasing the parameter z in Fig. 2), smaller nested elements would result into slightly smaller coupling efficiency. This is because a larger z would result in the mode field with a changed sign over a larger spatial region and thus a reduced overlap with the Gaussian field which is positive everywhere. For operation in the second window, this parameter will not have a significant impact on the coupling efficiency. Also influential is the role of the number of nested tubes. Again, for operation in the first window, the same argument leads us to conclude that coupling efficiency into the simple tubular

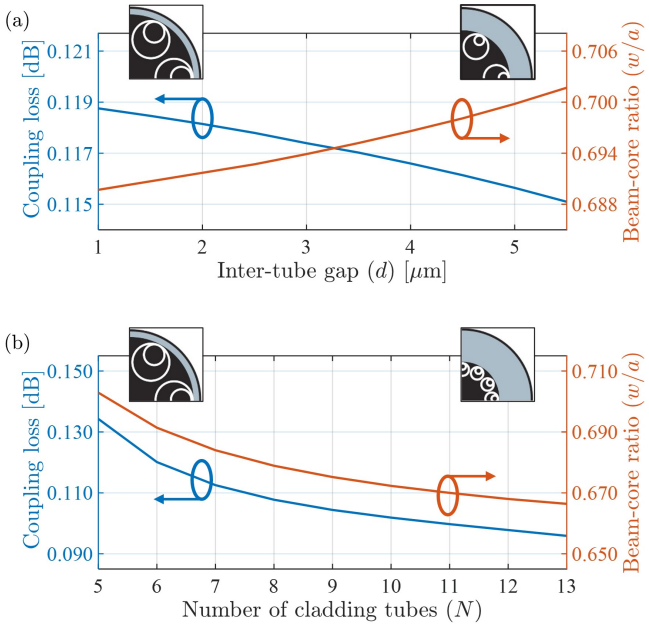

Fig. 5. Impact of the (a) inter-tube distance d and (b) number of cladding tubes on the coupling loss and the ideal beam-core ratio w/a. While both figures show a clear trend of the examined parameters on the coupling loss and beam-core ratio, they can also influence other properties of the HCF, e.g. the attenuation (see text). Note the different scaling of the y-axes for the two simulations – both performed in the first optical transmission window, corresponding to the normalized frequency of $f = 0.74$.

fibre would be the lowest. The NANF geometry improves this slightly as the field would change signs twice as it crosses the two membranes and a DNANF (c) would again see a slight decrease in coupling efficiency, although the difference would grow smaller as the number of nested tubes increases. Ultimately, we can conclude that for practical applications and in fibre structures which have shown great success so far, the most effective way of optimizing the coupling efficiency for a specific application is to operate in the second antiresonant window. In the following section, we verify these predictions by performing experimental measurements of two NANFs operating in the first and second antiresonant windows, respectively.

III. Experimental Measurements

To validate experimentally the predictions made from the foregoing analysis, we set out to measure the coupling efficiency of a laser beam into NANFs operating in first and second antiresonant windows. We assess the CEs at a given wavelength in two fibres with membrane thicknesses chosen so that the wavelength of operation is in the first and second window of the fibre samples, respectively. We developed a custom-setup to optimize the launch into the NANFs across all the degrees of freedom available. First we describe the fibres used, followed by introducing the experimental setup, and lastly we discuss the methodology of the measurements.

A. Fibre samples

For simplicity, the fibre samples used for the experiments will be referred to as NANF-1 (first window) and NANF-2 (second window) and the relevant data will be colour-coded with blue and red, respectively. To ensure the most accurate measurements possible and enable conclusive comparison with the theoretical analysis, the two fibre pieces; NANF-1 and NANF-2 were fabricated with very similar structural parameters except for the tube thickness, resulting in overlapping first and second transmission windows of the respective fibres. This allows measurement of the CE for both NANFs with the same laser source and coupling setup, which facilitates comparison between the two fibres.

TABLE I
Summary of the most relevant parameters of the NANF samples used for the experimental measurements

Parameter	NANF-1	NANF-2
Core diameter $[\mu m]$	30.0	29.4
Membrane thickness $[nm]$	~ 360	~ 750
Antiresonance window order for $\lambda_0 = 1064\,\text{nm}$	1^{st}	2^{nd}
Fundamental mode attenuation at $\lambda_0 = 1064\,\text{nm}$ $[dB/km]$	1.58 ± 0.13	0.35 ± 0.05
Corresponding propagation loss (PL) for $l_0 = 10\,\text{m}$ of fibre pieces [%]	0.4 ± 0.03	0.08 ± 0.01

For our purpose, it was necessary for the fibre samples to: (i) have the same symmetry. We made both fibres from a five-tube NANF preform. (ii) Have similar core diameters – this would be paramount in ensuring that the same focusing condition can be used for both fibres. (iii) Have comparable and low attenuation, and corresponding propagation loss (PL), and (iv) have the central wavelength λ_0 of the laser fall into different optical transmission windows of the respective fibre samples. When ideal coupling is achieved for either NANF-1 or NANF-2, the difference of $0.6\,\mu\text{m}$ in core diameter, will translate to an increased CL in the order of $< 0.002\,\text{dB}$ or $< 0.04\,\%$ relative difference – comparable to numerical error levels –, assuming identical coupling conditions, and such are neglected. Furthermore, the last criterion was achieved through changing the thickness of the cladding membranes. The main parameters for NANF-1 and NANF-2 are summarized in Table I, showing compliance with all the specifications above.

Figure 6 shows the loss spectra of both fibre samples evaluated via cutback measurements (from lengths of 850 m, and 2250 m each to 10 m for both NANF-1 and NANF-2, respectively) recorded using a white light source (WLS - Thorlabs SLS201L/M) and a broadband optical spectrum analyser (OSA - Ando AQ-6315A). After averaging, the transmitted spectra of several output cleaves – while the input coupling conditions were strictly maintained – the error bars can be calculated, as also presented in Table I. These shorter cutback pieces were then prepared to be 10 m long samples that will be used for the experimental verification measurements. The 5-tube NANF structure allows low FM attenuation whilst imposing high loss on all other HOMs and achieving an effectively single-mode operation after short propagation distances [35]. We determined from loss simulations of both fibre samples that an initial length of $l_0 = 10\,\text{m}$ together with optimum alignment would ensure effectively single-moded guidance,

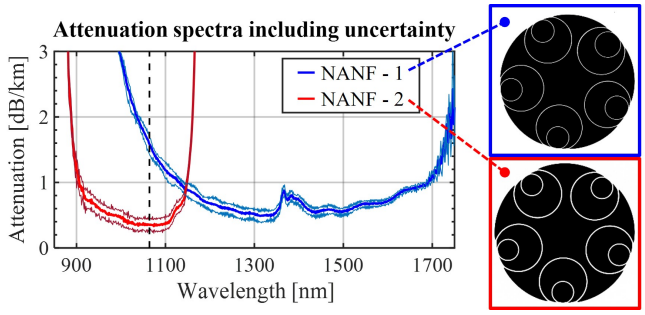

Fig. 6. Cutback measurements of the NANF samples used for the experiments. Following the colour convention, the blue and red curves show the attenuation of the 1^{st} (NANF-1) and the 2^{nd} (NANF-2) window fibres including the error bars covering the $900-1700$ nm wavelength range, respectively. The dashed vertical line marks the central wavelength $\lambda_0 = 1064$ nm of the laser source, while the SEMs of the fibre samples are presented on the right.

with negligible contribution of HOMs.

After capturing cross-section images of both fibers with a scanning electron microscope, we extracted their permittivity profiles and used as input to the finite element solver. We then computed the fiber modes – illustrated for NANF-2 in Figure 7 – and used Equation (3) to compute the corresponding CEs with a free space Gaussian beam as a function of its beam parameter. Our results for both fibers are shown in Figure 7. The slight asymmetry of the fiber structures induced by the fabrication process results in them supporting modes that are closer to the LP classification we adopted earlier but which also receive more power at the coupling point than the perfectly symmetric fibers.

For both fibres, the highest coupling efficiency is achieved for $w/a \approx 0.72$ due to the asymmetries in the structures. Within $\pm 2\,\%$ of this optimum w/a value, the calculated coupling efficiency changes by less than $0.01\,\%$, justifying our use of the same, unaltered coupling conditions (which was initially optimized to achieve maximal coupling into NANF-2) for both fibre pieces in the following experiments, despite the $2\,\%$ core diameter difference between the 2 fibers. More importantly, however, for this pair of fibres, our simulations predict a higher coupling efficiency for the fibre operating in the second window.

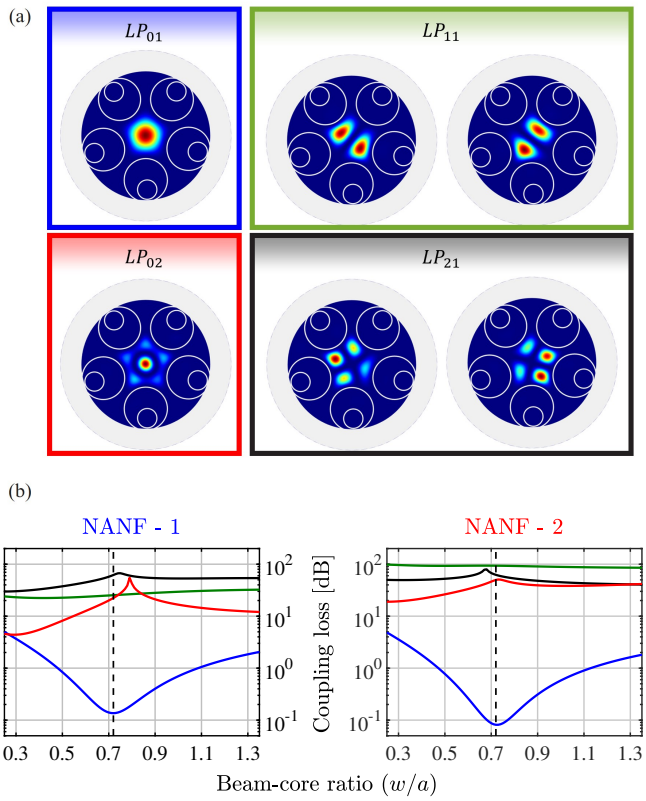

Fig. 7. (a) Illustrations of the normalized electric field distribution of the 6 vectors modes of the first 4 mode groups. The simulation is based on the SEM capture of NANF-2. (b) Corresponding coupling loss values of the respective mode groups, as a function of the beam-core ratio w/a. Compared to the ideal case (shown in Figure 2), the ideal coupling (marked with vertical dashed line) is slightly increased to a 0.72 beam-core ratio from 0.7. However, similar to the ideal simulations, under ideal coupling conditions, the coupling loss into the FM is ~2 order of magnitude lower when compared to the HOMs.

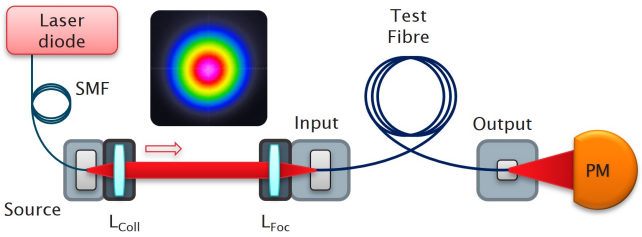

Fig. 8. Schematics of the experimental setup used to measure the CE. SMF: tightly coiled PM-980 mode filtering fibre loop, L_{Coll} and L_{Foc} are the collimating and focusing lens, respectively, PM: power meter. Inset: cross-section of the input beam waist. More specifications regarding the setup are detailed in the text.

B. Experimental setup

The setup we built to measure the coupling efficiency into the NANFs is schematically illustrated in Fig.8. The light source used is a single-mode Bookham LC96A diode laser emitting P_{avg} ~100 $\pm$ 0.7 mW average power in continuous wave operation mode. Its central wavelength is $\lambda_0 = 1064$ nm with $\Delta\lambda = 10$ nm spectral bandwidth. The output of the laser diode is connected to a commercially available PM-980 fibre with a tightly coiled section (~13 mm bending radius) to help filter out any residual light not coupled into its FM.

The output of this patchcord – terminated with a standard FC/APC connector – was mounted on top of an assembly consisting of a ThorLabs MicroBlock Stage and a compatible Pitch and Yaw (P'n'Y) platform. This enabled a 5-axis (3 XYZ translational + 2 P'n'Y rotational) alignment of the launch beam. After out-coupling from the delivery patch fibre, the divergent beam is collimated and then refocused using a pair of achromatic lenses, with focal lengths of $f_{Coll} = 10$ mm and $f_{Foc} = 50$ mm, respectively. This set of lenses was chosen such that after fine tuning optical distances between the respective elements of the system, the combined magnification on the source results in a beam waist that matches well with the theoretically predicted MFD of the NANF. The intensity profile of the focused beam recorded by a CMOS detector is

also shown as an inset on Figure 8.

After both end faces of the NANF samples were cleaved with a Fujikura precision cleaver – reliably and repeatedly achieving $< 0.3^\circ$ flat facet cleaves – the fibre tips were mounted on top of the 5-axis stage assembly described above. This stage made possible the best alignment conditions and ensured that the highest CE would be experimentally achieved. For all the measurements, the fibre samples were left in a loose coil of > 30 cm in diameter, ensuring that the macro-bending induced losses will be negligible.

At the output of the NANF samples, the power was recorded with a power meter. The exact installation of the output facet of the test NANFs showed no effect on the measurement results and therefore, a singular MicroStage without a P'n'Y component was sufficient. The P_{out} output and P_{in} input power was recorded by a ThorLabs photodiode power sensor.

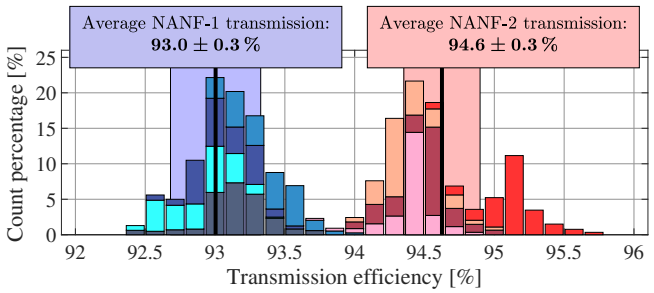

Fig. 9. Histogram representation of measured transmission efficiency values into NANF-1 and NANF-2. Each bin aggregates a range of 0.15 %. The y-axis covers the counts of transmission efficiency recorded for given bins for each fibre piece, blue and red for NANF-1 and NANF-2, respectively. The different colour shades illustrate the results from independent experimental conditions. The average across all measurements and confidence interval is highlighted with thick black lines and shaded backgrounds, while the corresponding numerical values are shown above the respective histograms. The uncertainties arise from the power fluctuations of the source.

C. Methodology

After the NANF samples were prepared and mounted on the alignment stages, we conducted the following experiments. All power measurements were recorded over a half-minute time window to ensure that the $< 0.7\,\%$ power fluctuations of the laser source were taken into account. After the P_{out} output power was collected for a given experiment, the fibre piece was dismounted and the power meter was placed after the coupling optics to measure the P_{in} input power, at a position after the focal position of the lens assembly, such that the beams incident in the 2 cases had identical spot sizes. This minimized any error related to the spot size and spot position on the detector surface. This procedure was repeated 4 times for both fibre samples, each time with a new input cleave, which practically meant an independent mounting condition. After each cleave, a slight re-alignment of the input fibre tip to the incoming beam was required to optimize the power throughput.

Since the measured P_{out}/P_{in} ratio also includes the propagation losses (PL), these also had to be considered. The coupling loss can be obtained by subtracting this PL from the measured loss values. Once the PL is accounted for, the calculated experimental results can be compared with the theoretical expectation, detailed in the next section.

IV. Results and Discussion

After recording the output power for four separate input cleaves, we calculated the transmission efficiency as the ratio between the reference input power P_{in} and the output power P_{out}. Figure 9 illustrates our measurement results in terms of the FM transmission efficiency of the fibre samples. In accordance with the color scheme described above, the results shaded in blue correspond to NANF-1 whiles those in red correspond to NANF-2. Moreover, the different hues indicates the results of separate measurements (input cleaves $1-4$). As mentioned in the Methodology section, each single measurement was recorded over a half minute time window, allowing to quantify the effect of the instability of the light source. After recording the power values over the mentioned 30 s time windows (~5000 sample points) for each cleave, we grouped the corresponding transmission efficiency values shown on the x-axis into 0.15 % wide bins for better visual representation. The count percentages along the y-axis refer to the number of occurrences of the given average transmission efficiency value of the bins, relative to the total number of sample points for the respective NANF. Records from different experimental conditions, i.e., fresh precision cleaves and re-optimized alignment, are contrasted by the distinct colours shown on the stacked bar chart. Highlighted on the labels are the average experimental results of $93.0 \pm 0.3\,\%$ and $94.6 \pm 0.3\,\%$ for NANF-1 and NANF-2, respectively (M-TE in Table II), showing an average difference of 1.6 p.p. or 1.7 % relative discrepancy in transmission efficiency. All relevant efficiency values discussed hereinafter are summarized in Table II.

The average coupling efficiency was then extracted from this by accounting for the average loss accrued after propagation over 10 m of fibre. The propagation efficiencies (including the uncertainties) were calculated from the values in Table I to be $99.6 \pm 0.03\,\%$ and $99.92 \pm 0.01\,\%$ for NANF-1 and NANF-2 – corresponding to 0.016 dB and 0.0035 dB average propagation losses – respectively (C-PE in Table II). It can be seen that the contribution of the attenuation can account for a measurable (~20 %) portion of the expected CE difference between the 2 fibres. Separating the losses experienced during propagation leads to the calculated coupling efficiency values of $93.3 \pm 0.3\,\%$ and $94.7 \pm 0.3\,\%$ for samples NANF-1 and NANF-2 (C-CE in Table II), respectively, showing an average difference of 1.4 p.p. or 1.5 % relative change.

We ascribe the difference between these measurements and our predictions from Figure 7 to the shape of the laser beam which is not an ideal Gaussian. To verify this hypothesis, we repeated the CEs calculations with the modes of the fibers, but this time using as incident beam the intensity profile captured on the CMOS camera placed after the coupling optics. The CE maxima from these simulation are 93.2 % and 94.5 %, for NANF-1 and NANF-2 (S-CE in Table II), respectively, indicating a difference of 1.3 p.p., or 1.4 %

TABLE II
SUMMARY TABLE OF THE RELEVANT EFFICIENCY VALUES FOR NANF-1 AND NANF-2, WITH THE LAST ROW COMPARING EXPERIMENTAL AND SIMULATION RESULTS

Efficiency values	NANF-1	NANF-2
Measured total transmission efficiency (M-TE) [%]	93.0 ± 0.3	94.6 ± 0.3
Calculated propagation efficiency (C-PE) [%]	99.64 ± 0.03	99.92 ± 0.01
Calculated coupling efficiency (C-CE) [%]	93.3 ± 0.3	94.7 ± 0.3
Simulated theoretical coupling efficiency (S-CE) [%]	93.2	94.5
	Simulations	Experiments
NANF-1 and NANF-2 coupling efficiency difference [p.p.]	1.3	1.4 ± 0.6

relative deviation. This better agreement with measurements confirms our hypothesis on the role of the shape of the incident beam.

The measured data and corresponding error-bars, calculated here assuming Gaussian error propagation through the data sets, are also shown in Table II. The ~1.4 p.p. (or 0.06 dB) average difference in the measured coupling efficiency between NANF-1 and NANF-2 is in excellent agreement with the predicted difference of 1.3 p.p. of our modelling, which could be also translated to a propagation loss over ~170 m in the latter fibre. This shows clearly that for applications requiring up to a few hundred meters of fibre, fibres operating in the second antiresonant window are preferable as they offer the lowest total loss, assuming similar other experimental conditions.

V. CONCLUSION

In summary, we have explored for the first time the fundamental limits on the efficiency with which laser beams with a circularly symmetric Gaussian profile couple into hollow-core antiresonant fibres which typically feature an N-fold symmetry (N being the number of sets of cladding tube, nested or otherwise). We saw that to good accuracy, a Gaussian beam with a beam waist $w \approx 70\,\%$ of the core radius a provides the maximum coupling efficiency to the fundamental mode of nodeless ARFs, providing a shorthand calculation for the mode field diameter. The $> 96\,\%$ coupling efficiency maxima we obtain from simulations are similar to those achievable for example in solid-core single-mode fibres [31].

Using the NANF structure as an example, we studied how key geometrical parameters defining the ARF geometry affect this maximum achievable coupling efficiency. Interestingly, we found that the most important parameter was the membrane thickness, observing that fibres operating in even-numbered windows achieve higher coupling efficiencies than those operating in odd-numbered windows, with the highest coupling efficiency $> 98\,\%$ achieved in the second antiresonant window. This effect, we found, originates from the fact that the guided mode field changes signs an even or odd number of times across the membrane depending on the order of the operating antiresonant window.

Setting out to verify this latter prediction experimentally, we measured the coupling efficiency into two nearly identical NANFs fabricated in-house and operating at 1064 nm in the first and second antiresonant windows, respectively. Experimentally, we achieved coupling efficiencies of $93.3 \pm 0.3\,\%$ and $94.7 \pm 0.3\,\%$ for the two fibres, respectively. The discrepancy between measured and simulated maximum values are due to asymmetries in the cross-section of the fibre, as well as in the profile of the experimental laser beam. Nevertheless, the results show a consistent ~1.4 p.p. higher coupling efficiency for the second window NANF.

The results presented in this paper show that using NANFs, and by extension other antiresonant fibres operating in their second antiresonant window, are the preferred choice for various applications where coupling efficiency into the fibres is critical. One such example is in laser power delivery, where hollow-core fibres promise to be a game changer [2]. In this application, optimizing the launch efficiency not only ensures delivering the maximum power from the source to the workpiece, but also helps simplify heat management and avert damage to the fibre by light not captured by the fibre's modes.

VI. ACKNOWLEDGEMENT

The authors would like to gratefully acknowledge the financial support of the Airguide Photonics Programme Grant EP/P030181, as well as the UKRI EPSRC 2278720 Project Grant.

REFERENCES

[1] G. T. Jasion, H. Sakr, J. R. Hayes, S. R. Sandoghchi, L. Hooper, E. Numkam Fokoua, A. Saljoghei, H. C. Mulvad, M. Alonso, A. Taranta, T. D. Bradley, I. A. Davidson, Y. Chen, D. J. Richardson, and F. Poletti, "0.174 dB/km Hollow Core Double Nested Antiresonant Nodeless Fiber (DNANF)," in *2022 Optical Fiber Communications Conference and Exhibition (OFC)*, Mar. 2022, pp. 1–3.

[2] H. C. H. Mulvad, S. Abokhamis Mousavi, V. Zuba, L. Xu, H. Sakr, T. D. Bradley, J. R. Hayes, G. T. Jasion, E. Numkam Fokoua, A. Taranta, S.-U. Alam, D. J. Richardson, and F. Poletti, "Kilowatt-average-power single-mode laser light transmission over kilometre-scale hollow-core fibre," *Nature Photonics*, pp. 1–6, May 2022, publisher: Nature Publishing Group. [Online]. Available: https://www.nature.com/articles/s41566-022-01000-3

[3] X. Zhu, X. Zhu, F. Yu, F. Yu, D. Wu, S. Chen, Y. Jiang, L. Hu, and L. Hu, "Laser-induced damage of an anti-resonant hollow-core fiber for high-power laser delivery at 1 μm," *Optics Letters*, vol. 47, no. 14, pp. 3548–3551, July 2022, publisher: Optica Publishing Group. [Online]. Available: https://opg.optica.org/ol/abstract.cfm?uri=ol-47-14-3548

[4] B. M. Masum, S. M. Aminossadati, M. S. Kizil, and C. R. Leonardi, "Numerical and experimental investigations of pressure-driven gas flow in hollow-core photonic crystal fibers," *Applied Optics*, vol. 58, no. 4, pp. 963–972, Feb. 2019, publisher: Optical Society of America. [Online]. Available: https://www.osapublishing.org/ao/abstract.cfm?uri=ao-58-4-963

[5] D. S. Bykov, O. A. Schmidt, T. G. Euser, and P. S. J. Russell, "Flying particle sensors in hollow-core photonic crystal fibre," *Nature Photonics*, vol. 9, no. 7, pp. 461–465, July 2015. [Online]. Available: https://www.nature.com/articles/nphoton.2015.94

[6] T. Morioka, Y. Awaji, R. Ryf, P. Winzer, D. Richardson, and F. Poletti, "Enhancing optical communications with brand new fibers," *IEEE Communications Magazine*, vol. 50, no. 2, pp. s31–s42, 2012, conference Name: IEEE Communications Magazine.

[7] E. Desurvire, C. Kazmierski, F. Lelarge, X. Marcadet, A. Scavennec, F. A. Kish, D. F. Welch, R. Nagarajan, C. H. Joyner, R. P. Schneider, S. W. Corzine, M. Kato, P. W. Evans, M. Ziari, A. G. Dentai, J. L. Pleumeekers, R. Muthiah, S. Bigo, M. Nakazawa, D. J. Richardson, F. Poletti, M. N. Petrovich, S. U. Alam, W. H. Loh, and D. N. Payne, "Science and technology challenges in XXIst century optical communications," *Comptes Rendus Physique*, vol. 12, no. 4, pp. 387–416, May 2011. [Online]. Available: https://www.sciencedirect.com/science/article/pii/S1631070511000922

[8] H. Sakr, Y. Chen, G. T. Jasion, T. D. Bradley, J. R. Hayes, H. C. H. Mulvad, I. A. Davidson, E. Numkam Fokoua, and F. Poletti, "Hollow core optical fibres with comparable attenuation to silica fibres between 600 and 1100 nm," *Nature Communications*, vol. 11, no. 1, p. 6030, Nov. 2020. [Online]. Available: https://www.nature.com/articles/s41467-020-19910-7

[9] louise, "euNetworks deploys Lumenisity® Limited CoreSmart® hollowcore fibre cable in London • euNetworks," Apr. 2021. [Online]. Available: https://eunetworks.com/news/eunetworks-deploys-lumenisity-limited-coresmart-hollowcore-fibre-cable-in-london/

[10] Z. Liu, B. Karanov, L. Galdino, J. R. Hayes, D. Lavery, K. Clark, K. Shi, D. J. Elson, B. C. Thomsen, M. N. Petrovich, D. J. Richardson, F. Poletti, R. Slavík, and P. Bayvel, "Nonlinearity-Free Coherent Transmission in Hollow-Core Antiresonant Fiber," *Journal of Lightwave Technology*, vol. 37, no. 3, pp. 909–916, Feb. 2019.

[11] A. Taranta, E. Numkam Fokoua, S. Abokhamis Mousavi, J. R. Hayes, T. D. Bradley, G. T. Jasion, and F. Poletti, "Exceptional polarization purity in antiresonant hollow-core optical fibres," *Nature Photonics*, vol. 14, no. 8, pp. 504–510, Aug. 2020, number: 8 Publisher: Nature Publishing Group. [Online]. Available: https://www.nature.com/articles/s41566-020-0633-x

[12] "Mitsubishi Heavy Industries, Ltd. Global Website | Technical Review." [Online]. Available: https://www.mhi.com/company/technology/review

[13] K. Shima, S. Ikoma, K. Uchiyama, Y. Takubo, M. Kashiwagi, and D. Tanaka, "5-kW single stage all-fiber Yb-doped single-mode fiber laser for materials processing," in *Fiber Lasers XV: Technology and Systems*, vol. 10512. International Society for Optics and Photonics, Feb. 2018, p. 105120C. [Online]. Available: https://www.spiedigitallibrary.org/conference-proceedings-of-spie/10512/105120C/5-kW-single-stage-all-fiber-Yb-doped-single-mode/10.1117/12.2287624.short

[14] F. Yu, P. Song, D. Wu, T. Birks, D. Bird, and J. Knight, "Attenuation limit of silica-based hollow-core fiber at mid-IR wavelengths," *APL Photonics*, vol. 4, no. 8, p. 080803, Aug. 2019, publisher: American Institute of Physics. [Online]. Available: https://aip.scitation.org/doi/10.1063/1.5115328

[15] M. A. Cooper, J. Wahlen, J. C. A. Zacarias, D. C. Delgado, I. Divliansky, J. Antonio-Lopez, A. Schulzgen, and R. A. Correa, "KW single mode CW laser transmission in an anti-resonant hollow-core fiber," in *Laser Technology for Defense and Security XVII*, vol. PC12092. SPIE, May 2022, p. PC120920C. [Online]. Available: https://www.spiedigitallibrary.org/conference-proceedings-of-spie/PC12092/PC120920C/KW-single-mode-CW-laser-transmission-in-an-anti-resonant/10.1117/12.2619034.full

[16] M. Michieletto, J. K. Lyngsø, C. Jakobsen, J. Lægsgaard, O. Bang, and T. T. Alkeskjold, "Hollow-core fibers for high power pulse delivery," *Optics Express*, vol. 24, no. 7, pp. 7103–7119, Apr. 2016, publisher: Optical Society of America. [Online]. Available: https://www.osapublishing.org/oe/abstract.cfm?uri=oe-24-7-7103

[17] I. A. Bufetov, A. N. Kolyadin, A. F. Kosolapov, V. P. Efremov, and V. E. Fortov, "Catastrophic damage in hollow core optical fibers under high power laser radiation," *Optics Express*, vol. 27, no. 13, pp. 18 296–18 310, June 2019. [Online]. Available: https://www.osapublishing.org/oe/abstract.cfm?uri=oe-27-13-18296

[18] B. Siwicki, R. M. Carter, J. D. Shephard, F. Yu, J. C. Knight, and D. P. Hand, "Negative-Curvature Anti-Resonant Fiber Coupling Tolerances," *Journal of Lightwave Technology*, vol. 37, no. 21, pp. 5548–5554, Nov. 2019, conference Name: Journal of Lightwave Technology.

[19] Y. Cui, Y. Cui, W. Huang, W. Huang, Z. Zhou, Z. Zhou, H. Li, H. Li, M. Wang, M. Wang, M. Wang, Z. Chen, Z. Chen, Z. Chen, Z. Wang, Z. Wang, and Z. Wang, "Highly efficient and stable coupling of kilowatt-level continuous wave laser into hollow-core fibers," *Chinese Optics Letters*, vol. 20, no. 4, p. 040602, Apr. 2022, publisher: Chinese Optical Society. [Online]. Available: https://opg.optica.org/col/abstract.cfm?uri=col-20-4-040602

[20] C. Goel, H. Li, M. R. A. Hassan, W. Chang, and S. Yoo, "Anti-resonant hollow-core fiber fusion spliced to laser gain fiber for high-power beam delivery," *Optics Letters*, vol. 46, no. 17, pp. 4374–4377, Sept. 2021, publisher: Optical Society of America. [Online]. Available: https://www.osapublishing.org/ol/abstract.cfm?uri=ol-46-17-4374

[21] M. Komanec, D. Suslov, S. Zvánovec, Y. Chen, T. Bradley, S. R. Sandoghchi, E. R. Numkam Fokoua, G. T. Jasion, M. N. Petrovich, F. Poletti, D. J. Richardson, and R. Slavík, "Low-Loss and Low-Back-Reflection Hollow-Core to Standard Fiber Interconnection," *IEEE Photonics Technology Letters*, vol. 31, no. 10, pp. 723–726, 2019, conference Name: IEEE Photonics Technology Letters.

[22] D. Suslov, M. Komanec, E. R. Numkam Fokoua, D. Dousek, A. Zhong, S. Zvánovec, T. D. Bradley, F. Poletti, D. J. Richardson, and R. Slavík, "Low loss and high performance interconnection between standard single-mode fiber and antiresonant hollow-core fiber," *Scientific Reports*, vol. 11, no. 1, p. 8799, Apr. 2021, number: 1 Publisher: Nature Publishing Group. [Online]. Available: https://www.nature.com/articles/s41598-021-88065-2

[23] S. Xie, R. Pennetta, and P. S. J. Russell, "Self-alignment of glass fiber nanospike by optomechanical back-action in hollow-core photonic crystal fiber," *Optica*, vol. 3, no. 3, pp. 277–282, Mar. 2016. [Online]. Available: https://www.osapublishing.org/optica/abstract.cfm?uri=optica-3-3-277

[24] X. Chen, X. Hu, L. Liao, Y. Xing, G. Chen, L. Yang, J. Peng, H. Li, N. Dai, and J. Li, "High coupling efficiency technology of large core hollow-core fiber with single mode fiber," *Optics Express*, vol. 27, no. 23, pp. 33 135–33 142, Nov. 2019, publisher: Optical Society of America. [Online]. Available: https://www.osapublishing.org/oe/abstract.cfm?uri=oe-27-23-33135

[25] E. N. Fokoua, R. Slavik, D. J. Richardson, and F. Poletti, "Limits of Coupling Efficiency into Hollow-Core Antiresonant Fibers," in *Conference on Lasers and Electro-Optics (2021), paper STu1Q.4*. Optica Publishing Group, May 2021, p. STu1Q.4. [Online]. Available: https://opg.optica.org/abstract.cfm?uri=CLEO_SI-2021-STu1Q.4

[26] T. D. Bradley, J. R. Hayes, Y. Chen, G. T. Jasion, S. R. Sandoghchi, R. Slavik, E. N. Fokoua, S. Bawn, H. Sakr, I. Davidson, A. Taranta, J. P. Thomas, M. N. Petrovich, D. Richardson, and F. Poletti, "Record Low-Loss 1.3dB/km Data Transmitting Antiresonant Hollow Core Fibre," in *2018 European Conference on Optical Communication (ECOC)*, Sept. 2018, pp. 1–3.

[27] V. Zuba, H. C. H. Mulvad, R. Slavík, H. Sakr, F. Poletti, D. J. Richardson, and E. N. Fokoua, "Experimental Investigation into Optimum Laser Coupling Efficiency into Hollow-Core NANFs," in *Conference on Lasers and Electro-Optics (2022), paper SW4K.1*. Optica Publishing Group, May 2022, p. SW4K.1. [Online]. Available: https://opg.optica.org/abstract.cfm?uri=CLEO_SI-2022-SW4K.1

[28] S. Johnson, M. Ibanescu, M. Skorobogatiy, O. Weisberg, T. Engeness, M. Soljacic, S. Jacobs, J. Joannopoulos, and Y. Fink, "Low-loss asymptotically single-mode propagation in large-core OmniGuide fibers," *Optics Express*, vol. 9, no. 13, p. 748, 2001. [Online]. Available: https://www.osapublishing.org/oe/abstract.cfm?uri=oe-9-13-748

[29] R. Sammut and A. W. Snyder, "Leaky modes on a dielectric waveguide: orthogonality and excitation," *Applied Optics*, vol. 15, no. 4, pp. 1040–1044, Apr. 1976, publisher: Optica Publishing Group. [Online]. Available: https://opg.optica.org/ao/abstract.cfm?uri=ao-15-4-1040

[30] W.-P. Huang and J. Mu, "Complex coupled-mode theory for optical waveguides," *Optics Express*, vol. 17, no. 21, pp. 19 134–19 152, Oct. 2009, publisher: Optica Publishing Group. [Online]. Available: https://opg.optica.org/oe/abstract.cfm?uri=oe-17-21-19134

[31] D. Marcuse, "Loss analysis of single-mode fiber splices," *Bell System Technical Journal*, vol. 56, no. 5, pp. 703–718, 1977. [Online]. Available: https://onlinelibrary.wiley.com/doi/abs/10.1002/j.1538-7305.1977.tb00534.x

[32] P. Uebel, M. C. Günendi, M. H. Frosz, G. Ahmed, N. N. Edavalath, J.-M. Ménard, and P. S. J. Russell, "Broadband robustly single-mode hollow-core PCF by resonant filtering of higher-order modes," *Optics Letters*, vol. 41, no. 9, pp. 1961–1964, May 2016, publisher: Optica Publishing Group. [Online]. Available: https://opg.optica.org/ol/abstract.cfm?uri=ol-41-9-1961

[33] H. Sakr, T. D. Bradley, G. T. Jasion, E. Numkam Fokoua, S. R. Sandoghchi, I. A. Davidson, A. A. Taranta, G. Guerra, W. Shere, Y. Cheng, J. R. Hayes, D. J. Richardson, and F. Poletti, "Hollow Core NANFs with Five Nested Tubes and Record Low Loss at 850, 1060, 1300 and 1625nm | IEEE Conference Publication | IEEE Xplore," July 2021. [Online]. Available: https://ieeexplore.ieee.org/abstract/document/9489469

[34] W. Shere, E. N. Fokoua, G. T. Jasion, and F. Poletti, "Designing multi-mode anti-resonant hollow-core fibers for industrial laser power delivery," *Optics Express*, vol. 30, no. 22, pp. 40 425–40 440,

Oct. 2022, publisher: Optica Publishing Group. [Online]. Available: https://opg.optica.org/oe/abstract.cfm?uri=oe-30-22-40425

[35] H. Sakr, T. D. Bradley, G. T. Jasion, E. Numkam Fokoua, S. R. Sandoghchi, I. A. Davidson, A. Taranta, G. Guerra, W. Shere, Y. Chen, J. R. Hayes, D. J. Richardson, and F. Poletti, "Hollow core nanfs with five nested tubes and record low loss at 850, 1060, 1300 and 1625nm," in *2021 Optical Fiber Communications Conference and Exhibition (OFC)*, 2021, pp. 1–3.